Exploring the Magnetic Phase Diagram and Hall Resistivity Suppression in Centrosymmetric $GdOs_2Si_2$ Single Crystal

Hiroaki Hayashi,[1,2,*] Moyu Kato,[3] Taichi Terashima,[1] Naoki Kikugawa,[4] Hiroya Sakurai,[1] Hiroyuki K. Yoshida,[3] Kazunari Yamaura [1,2]

[1] Research Center for Materials Nanoarchitectonics, National Institute for Materials Science, 1-1 Namiki, Tsukuba, Ibaraki 305-0044, Japan

[2] Graduate School of Chemical Sciences and Engineering, Hokkaido University, North 10 West 8, Kita-ku, Sapporo, Hokkaido 060-0810, Japan

[3] Department of Physics, Hokkaido University, North 10 West 8, Kita-ku, Sapporo, Hokkaido 060-0810, Japan

[4] Research Center for Energy and Environmental Materials, National Institute for Materials Science, 3-13 Sakura, Tsukuba, Ibaraki 305-0003, Japan

Magnetic skyrmions were initially identified in non-centrosymmetric materials. However, recent theoretical advancements have suggested their potential emergence in centrosymmetric compounds, which has been experimentally observed in cases such as $GdRu_2Si_2$. In this study, we comprehensively explored the magnetic properties of $GdOs_2Si_2$, a centrosymmetric counterpart to $GdRu_2Si_2$, with a focused investigation into the crystal direction-dependent behavior of key parameters. By combining magnetic, thermal, and transport measurements, we constructed a detailed magnetic phase diagram along two crystal directions, revealing intriguing similarities and differences compared to $GdRu_2Si_2$. Notably, we observed a distinct suppression of the Hall resistivity in $GdOs_2Si_2$—a phenomenon absent in its counterpart compound.

1. Introduction

Initially, magnetic skyrmions were observed only in materials without crystallographic inversion centers. Examples include MnSi, EuPtSi, and FeGe, where the Dzyaloshinski-Moriya interaction plays a pivotal role in magnetism [1–5]. However, theoretical advancements have proposed the possibility of skyrmion formation even in compounds with centrosymmetry [6–11]. For instance, in J_1-J_2(J_3) triangular-lattice antiferromagnets, geometrical frustration was predicted to lead to the emergence of skyrmion lattices, despite these systems being insulating,

unlike their predecessors [12]. Additionally, skyrmions observed in the Gd^{3+} triangular lattices in Gd_2PdSi_3 [13–16] and the breathing kagome networks in $Gd_3Ru_4Al_{12}$ [17–19] further support the influence of this magnetic frustration.

More recently, it has been suggested that the skyrmion lattice may also manifest in non-frustrated lattices with centrosymmetry and metallic attributes. The interplay between the Ruderman-Kittel-Kasuya-Yoshida (RKKY) interaction and multiple spin interaction is considered crucial in this context. This possibility was demonstrated in studies of the tetragonal compound $GdRu_2Si_2$ [20–25]. These findings suggest the ubiquitous presence of skyrmions across a variety of material systems.

Another important aspect of the skyrmion lattice is its characteristic transport properties. In particular, the topological Hall effect manifests itself in connection with the skyrmion lattice [1,26–28] due to the scalar spin chirality $S_i \cdot (S_j \times S_k)$, which acts like a fictitious magnetic field. However, only a few metallic compounds with spatial inversion symmetry currently studied show the existence of a skyrmion lattice [16,19–21,29]. Among them, $GdRu_2Si_2$ and $EuAl_4$ have attracted great attention due to their multi-Q-skirmion lattice and complex magnetic phase diagram [29,30].

In this study, we shift our focus to $GdOs_2Si_2$ [31,32], an osmium-substituted variant of $GdRu_2Si_2$. While the magnetic properties of $GdOs_2Si_2$ remain unresolved, it shares the centrosymmetry and layered structure stacking along the c-axis with $GdRu_2Si_2$. Given the slight variations in lattice constants and energy levels in the 4d and 5d electron bands between $GdOs_2Si_2$ and $GdRu_2Si_2$, one can reasonably anticipate differences in the nature of the Gd-spin interaction in these two compounds. Consequently, the magnetic phase diagram of $GdOs_2Si_2$ may also exhibit some alterations. We have meticulously summarized our measurements of $GdOs_2Si_2$ single crystals, including electrical resistivity, magnetization, and specific heat capacity. These results were compiled into a temperature-field phase diagram and juxtaposed with the phase diagram obtained for $GdRu_2Si_2$. The results show that there is a new magnetic phase in $GdOs_2Si_2$, which has not been observed before, and that the Hall resistivity is significantly suppressed in this phase.

2. Experimental

The crystal growth process of $GdOs_2Si_2$ was meticulously documented in a conference proceeding [31]. For the purposes of our study, we selected two crystals from the aforementioned batch, one of which is visually presented in Fig. S1 [33]. To definitively

establish the crystal's identity as $GdOs_2Si_2$, characterized by a $ThCr_2Si_2$-type structure with body-centered tetragonal symmetry (*I*4/*mmm*, #139) [31], an in-depth Laue X-ray diffraction analysis was conducted. The determination of crystal axes was carried out employing the same Laue method. Subsequently, the resultant lattice constants were determined to be a = 4.1549(2) Å and c = 9.8117(8) Å. These values exhibit a moderate decrease in a and a substantial increase in c when compared to the dimensions observed in $GdRu_2Si_2$ [a = 4.164(2) Å, c = 9.616(5) Å] [34].

We conducted measurements of magnetic, thermal, and transport properties across a temperature range spanning from 2 K to 300 K, as well as under varying magnetic fields (H), utilizing a single crystal sample. Initially, a slender plate-shaped crystal with approximate dimensions of 1.1 mm × 0.50 mm × 0.23 mm was chosen for the study. Additionally, to explore sample dependence, another crystal underwent similar investigations. A SQUID magnetometer, specifically the MPMS3 model from Quantum Design Inc., was utilized to collect magnetic data. The temperature-dependent magnetization (M) was recorded under field cooling conditions, and the magnetic susceptibility was calculated as $\chi = M/H$. To determine the specific heat capacity (C_p), the heat relaxation method was employed, with a magnetic field applied parallel to the c-axis. This measurement setup employed a commercially available system, specifically the PPMS model from Quantum Design Inc.

For the assessment of longitudinal resistivity (ρ_{xx}) and Hall resistivity (ρ_{yx}) (equal to -ρ_{xy}), a magnetic field parallel to the c-axis was applied using the transport option of the PPMS system. To secure the gold wires onto the crystal, silver paste was utilized, with the distance between the voltage terminals of the crystal set at 0.35 mm for ρ_{xx} and 0.38 mm for ρ_{yx} for the first crystal. Throughout these measurements, an excitation current of 20 mA was passed along the crystal's [100] direction.

3. Results and Discussion

Figure 1(a) shows the temperature dependence of χ curves (left) and their differentials dχ/dT curves (right) measured at various magnetic fields below 40 K. For the case of H//[001], distinct features labeled as T_1 (arrow), T_2 (triangle), and T_3 (diamond) were observed at different temperatures, corresponding to the peak positions in the dχ/dT curves. While the change at T_1 seems relatively smaller compared to the more pronounced peak-like changes at T_2 and T_3 in the differential curves, it becomes evident from the data at $\mu_0 H$ = 2.4 T and 3 T that T_1 and T_2 are indeed clearly separated at elevated magnetic fields. T_2 displays a more pronounced

decrease than T_1 as the magnetic field increases from 25 K (at $\mu_0 H$ = 1 T) to 6 K (at 3 T). Moreover, an anomaly emerges around 13 K at $\mu_0 H$ = 2 T (T_3), which fades as the magnetic field is further increased.

Regarding the situation where H//[100], at least two distinct changes were identified, as portrayed in Fig. 1(b). Although the overall profile of alterations appears to display a more gradual and uniform trend, qualitatively similar associations with temperature and magnetic field can be observed. For the sake of convenience, we label the temperatures corresponding to these distinctive changes as T_4 and T_5.

The upper portion of Fig. 2(a) shows the isothermal magnetization curve and its derivative curve obtained at 1.8 K while applying a magnetic field perpendicular to the crystal's c-plane (H//[001]). Within this depiction, the magnetization process demonstrates swift alterations at specific magnetic field strengths: $\mu_0 H_1$ = 2.5 T, $\mu_0 H_2$ = 2.8 T, and $\mu_0 H_3$ = 3.2 T, along with a gradual kink manifesting at $\mu_0 H_4$ = 6.5 T. These variations manifest more prominently within the differential curves. Notably, the transformations at H_1, H_2, and H_3 exhibit hysteresis in response to the magnetic field, underscoring their connection with first-order phase transitions. Conversely, the absence of noticeable hysteresis is evident at H_4, where the magnetization of Gd^{3+} ions achieves saturation at a value of 7 μ_B.

The outcomes of the measurements capturing magnetic transitions driven by varying temperatures and magnetic fields are presented in the lower section of Fig. 2(a). Notably, all transition fields—designated as H_1, H_2, H_3, and H_4—shift towards lower magnetic field strengths as the temperature increases. Specifically, H_3 diminishes around 10 K, while H_1 either merges with H_2 or vanishes entirely at approximately 20 K. As for H_4, it becomes progressively less distinguishable at elevated temperatures and is indiscernible beyond 20 K. This behavior can be attributed to the fact that, as elucidated later, the phase boundaries above 20 K align nearly perpendicular to the temperature axis.

At the upper section of Fig. 2(b), we present the M-H and dM/dH-H curves at 1.8 K, considering an external magnetic field aligned with H//[100]. When examining the H//[100] configuration, distinct anomalies are observed in the dM/dH curve at specific magnetic fields: $\mu_0 H_5$ = 1.1 T, $\mu_0 H_6$ = 2.5 T, $\mu_0 H_7$ = 5.7 T, and $\mu_0 H_8$ = 6.8 T. Notably, the anomaly at H_5 exhibits hysteresis. Moreover, a broader peak anomaly is noticeable in the dM/dH curve at H_6. In contrast, a well-defined peak manifests at H_7, positioned just slightly below the saturation field H_8. The prominence of this peak increases with rising temperature, as illustrated in the lower portion of Fig. 2(b). With increasing temperature, these critical fields shift towards lower

magnetic field values.

The phase diagram for H//[001] (left) and H//[100] (right) was established based on χ-T and M-H measurements, as illustrated in Fig. 3. The diagram features notable points such as T_1, T_2, T_3, H_1, H_2, H_3, and H_4, along with T_4, T_5, H_5, H_6, H_7, and H_8. In the H//[001] phase diagram, it is evident that four distinct magnetic phases (I, II, II', and III) exist before reaching saturation, contingent upon temperature and magnetic field conditions. The overall structure of this phase diagram closely resembles that of $GdRu_2Si_2$ [30], except for the possible inclusion of the phase II'.

To better understand the magnetic structure, longitudinal resistivity, ρ_{xx}, and Hall resistivity, ρ_{yx}, measurements were performed, and the results are shown in Fig. 4. Clear changes are observed at H_1, H_2, H_3, and H_4 for ρ_{xx} and ρ_{yx}, indicating a robust interaction between the local moment of Gd^{3+} and the conduction electrons. The magnetic field dependence is similar to that of $GdRu_2Si_2$ [21], except for phase II'. In particular, the prominent anomaly of ρ_{xx} and anomalous Hall effect of ρ_{yx} and σ_{yx} (see Fig. S2) [35] observed in phase II closely resembles the topological Hall effect observed in the double-Q square skyrmion lattice state of $GdRu_2Si_2$. Although skyrmion formation is theoretically predicted in $GdOs_2Si_2$ [36], our analysis did not successfully extract the topological Hall component by subtracting normal and anomalous Hall terms using $\rho_{yx} = \rho_{yx}^{N} + \rho_{yx}^{A} + \rho_{yx}^{T}$ (see Fig. S3) [37]. This limitation may stem from the crucial roles played by both real-space and momentum-space Berry curvature in the transverse motion of conduction electrons atop topological magnetic textures with relatively short periods, as discussed in previous studies [38,39]. The analysis method, which assumes scattering by a single skyrmion, may therefore be inadequate for application to $GdOs_2Si_2$, expected to involve a crossover between real-space and momentum-space descriptions.

On the other hand, the anomalous Hall effect in ρ_{yx} is suddenly suppressed, while ρ_{xx} sharply drops at H_2, with the minimum value of ρ_{xx} observed in Phase II'. Such a minimum value of ρ_{xx} and a drastic change of ρ_{yx} have not been identified in $GdRu_2Si_2$. This change is attributed to a rearrangement of the band structure near the Fermi surface due to the substitution of Os for Ru, resulting in a modification of the RKKY interactions between Gd ions. Consequently, the characteristic aspect of $GdOs_2Si_2$ is the II' phase, representing a magnetic state with an undisclosed spin configuration. Recent theoretical studies have suggested the existence of a topologically trivial double-Q state in the immediate vicinity of the double-Q square skyrmion lattice state [40]. The emergence of a topologically trivial spin texture, the meron-antimeron pair state, has been reported in $GdRu_2Ge_2$ [41]. The phase II' observed here

may reflect such a state, but further microscopic techniques are needed to accurately evaluate the exact magnetic structure.

In the study for H//[100], the existence of four magnetically ordered phases is suggested, namely phases I, III', IV, and V, which are qualitatively similar to those reported for $GdRu_2Si_2$ [30]. In $GdRu_2Si_2$, these phases are associated with anisotropic double-Q states (screw + sinusoidal), anisotropic double-Q states associated with a double-Q square vortex lattice, single Q-screw states, and single Q-fan states [30]. While it remains to be confirmed whether these states directly apply to $GdOs_2Si_2$, it is suggested that phase I of $GdOs_2Si_2$ extends closer to the boundary of the paramagnetic region and is potentially more stable than phase I of $GdRu_2Si_2$ [30]. In contrast, phase V only exists in the high-field part of the phase diagram and ceases well below the zero-field antiferromagnetic transition temperature. This persists even when the magnetic field is no longer small, continuing almost up to the zero-field transition temperature. The differences in these quantitative changes are likely attributed to variations in the strength of the magnetic interaction between the respective Gd^{3+} moments in $GdRu_2Si_2$ and $GdOs_2Si_2$.

The temperature dependence of C_p at zero magnetic field is shown in Fig. 5 (inset), where a distinct λ-type anomaly is observed at T_1. Since the isostructural nonmagnetic compounds usually used to separate the lattice contribution from the C_p data were not available, we attempted to analyze the data using the Einstein and Debye models: $C_p = \gamma T + C_E + C_D$. In this equation, the first term represents the conduction electron contribution and γ is the Sommerfeld coefficient. The second and third terms correspond to the phonon contribution according to the Einstein and Debye models and are given by:

$$C_E = 3n_E R \frac{x e^x}{(e^x-1)^2}$$

and

$$C_D = 9n_D R \left(\frac{T}{\theta_D}\right)^3 \int_0^{\theta_D/T} \frac{y^4 e^y}{(e^y-1)^2} \ ,$$

where $x = \theta_E/T$, $y = \theta_D/T$, θ_E and θ_D are the Einstein and Debye temperatures, respectively. The scale factors n_E and n_D correspond to the number of vibrational modes per formula unit for the Einstein and Debye models, respectively, so we applied the constraint $n_E + n_D = 5$. Fitting these equations yielded γ = 24.4(9) mJ mol^{-1}, n_E = 2.44(5), n_D = 2.55(5), θ_E = 142(2) K, and θ_D = 609(9) K.

Furthermore, the magnetic specific heat (C_{mag}) of $GdOs_2Si_2$ was obtained by

subtracting the contributions of conduction electrons and lattice vibrations from the C_p data, as shown in Fig. 5. The behavior of C_{mag} decreases rapidly as the temperature passes T_1. A broad hump then appears, and eventually, C_{mag} approaches zero in the low-temperature limit. Similar humps have been observed in other Gd compounds in the temperature range below the magnetic transition temperature [42]. It has been argued that a peak like this appears at approximately 1/4 of magnetic transition temperatures, based on a mean-field model, originating from the splitting of the Gd^{3+} ground-state multiplet due to an internal field [43–45].

It is important to note that in the ρ_{xx} vs T measurements, negative magnetoresistance, indicative of magnetic precursor effects, was observed above T_1 (Fig. S4) [46]. However, the broad peak of C_{mag} at high temperatures, characteristic of the magnetic precursor effect [47], was not clearly observed. The calculated magnetic entropy S_{mag} = 15.7 J mol^{-1} K^{-1} is slightly smaller than the theoretical value $R\ln(2J+1)$ = 17.3 J mol^{-1} K^{-1} (J = 7/2). This discrepancy may have been due to the limited temperature range in the analysis, which may have affected the fitting process.

Magnetic transitions at T_1, T_2, and T_3 are discernible in the C_{mag} curves when a magnetic field is aligned parallel to [001], as depicted in Fig. S5 [48]. Notably, C_{mag} exhibits sharp increases at both T_1 and T_2, signifying distinct phase transitions. However, while the magnetization notably decreases at T_3, there is no significant change observed in the C_{mag} curves. This outcome indicates the relatively minor entropy change associated with the phase transition occurring at T_3.

In addition, we conducted similar measurements on another crystal of $GdOs_2Si_2$ to explore the crystal-dependent aspects of the magnetic phase diagram. In this supplementary investigation, we observed slight variations in the magnetic transition temperatures. These subtle differences could be attributed to undetected disorder related to the distribution of elements between crystallographic sites within the $ThCr_2Si_2$-type structure [49], which can be challenging to assess using conventional X-ray diffraction methods. Furthermore, we examined the magnetic field dependence and noted some distinctions. However, these variations did not induce intrinsic and substantial changes in the overall structure of the magnetic phase diagram (detailed results can be found in Fig. S6) [50]. This suggests that the II and II' phases, which are expected to be associated with the appearance of the skyrmion lattice, represent stable intrinsic phases of the $GdOs_2Si_2$ crystal and are not easily disrupted by minor crystallographic disturbances.

4. Conclusion

This study presents the results obtained from investigating $GdOs_2Si_2$ using a single crystal, leading to the construction of a magnetic phase diagram along *H*//[100] and *H*//[001], revealing notable similarities with the phase diagram of $GdRu_2Si_2$. Of particular interest is the distinct Hall resistivity anomaly observed in phase II, reminiscent of the topological Hall effect seen in the skyrmion state of $GdRu_2Si_2$. This intriguing parallel suggests the potential occurrence of skyrmion formation in phase II of $GdOs_2Si_2$. Additionally, our investigation unveils an unrecognized phase (phase II') absent in $GdRu_2Si_2$. The appearance of this phase coincides with a distinct recovery pattern in the Hall resistivity, implying a significant shift in the spin structure. An in-depth understanding of the complex magnetic configurations in $GdOs_2Si_2$ could be facilitated by future endeavors involving advanced microscopic techniques like resonant X-ray diffraction measurements and the direct observation of possible skyrmions through electron microscopy.

Acknowledgment

We gratefully acknowledge the support of the World Premier International Research Center Initiative (WPI) of MEXT, Japan, which has enabled the contributions of MANA to this research. We extend our appreciation to H. Nakao (KEK, Japan) and Y. Tsujimoto (NIMS, Japan) for their invaluable discussions. This research has been partially funded by a Grant-in-Aid for Scientific Research from the Japan Society for the Promotion of Science (No. JP22H04601), as well as the Kazuchika Okura Memorial Foundation (No. 2022-11) and the Casio Science Promotion Foundation (39-10).

*E-mail: hhayashi@issp.u-tokyo.ac.jp

[1] A. Neubauer, C. Pfleiderer, B. Binz, A. Rosch, R. Ritz, P. G. Niklowitz, and P. Böni, Phys. Rev. Lett. **102**, 186602 (2009).

[2] X. Z. Yu, N. Kanazawa, Y. Onose, K. Kimoto, W. Z. Zhang, S. Ishiwata, Y. Matsui, and Y. Tokura, Nat. Mater. **10**, 106 (2011).

[3] N. Kanazawa, J.-H. Kim, D. S. Inosov, J. S. White, N. Egetenmeyer, J. L. Gavilano, S. Ishiwata, Y. Onose, T. Arima, B. Keimer, and Y. Tokura, Phys. Rev. B **86**, 134425 (2012).

[4] A. Bogdanov and A. Hubert, J. Magn. Magn. Mater. **138**, 255 (1994).

[5] M. Kakihana, D. Aoki, A. Nakamura, F. Honda, M. Nakashima, Y. Amako, T. Takeuchi, H. Harima, M. Hedo, T. Nakama, and Y. Ōnuki, J. Phys. Soc. Jpn. **88**, 094705 (2019).

[6] S. Z. Lin and S. Hayami, Phys. Rev. B **93**, 064430 (2016).

[7] S. Hayami, R. Ozawa, and Y. Motome, Phys. Rev. B **95**, 224424 (2017).

[8] R. Ozawa, S. Hayami, and Y. Motome, Phys. Rev. Lett. **118**, 147205 (2017).

[9] Z. Wang, Y. Su, S. Z. Lin, and C. D. Batista, Phys. Rev. Lett. **124**, 207201 (2020).

[10] S. Hayami and Y. Motome, Phys. Rev. B **103**, 024439 (2021).

[11] A. O. Leonov and M. Mostovoy, Nat. Commun. **6**, 8275 (2015).

[12] T. Okubo, S. Chung, and H. Kawamura, Phys. Rev. Lett. **108**, 017206 (2012).

[13] P.A. Kotsanidis, J.K. Yakinthos, and E. Gamari-Seale, J. Magn. Magn. Mater. **87**, 199 (1990).

[14] R. Mallik, E. V. Sampathkumaran, P. L. Paulose, H. Sugawarat, and H. Sato, Pramana - J. Phys. **51**, 505 (1998).

[15] S. R. Saha, H. Sugawara, T. D. Matsuda, H. Sato, R. Mallik, and E. V. Sampathkumaran, Phys. Rev. B **60**, 12162 (1999).

[16] T. Kurumaji, T. Nakajima, M. Hirschberger, A. Kikkawa, Y. Yamasaki, H. Sagayama, H. Nakao, Y. Taguchi, T. Arima, and Y. Tokura, Science **365**, 914 (2019).

[17] R. E. Gkandyshevskii, O. R. Strusievicz, K. Cenzual, and E. Parthe, Acta Cryst. B**49**, 474 (1993).

[18] V. Chandragiri, K. K. Iyer, and E. V. Sampathkumaran, J. Phys. Condens. Matter **28**, 286002 (2016).

[19] M. Hirschberger, T. Nakajima, S. Gao, L. Peng, A. Kikkawa, T. Kurumaji, M. Kriener, Y. Yamasaki, H. Sagayama, H. Nakao, K. Ohishi, K. Kakurai, Y. Taguchi, X. Yu, T. Arima, and Y. Tokura, Nat. Commun. **10**, 5831 (2019).

[20] Y. Yasui, C. J. Butler, N. D. Khanh, S. Hayami, T. Nomoto, T. Hanaguri, Y. Motome, R. Arita, T. Arima, Y. Tokura, and S. Seki, Nat. Commun. **11**, 5925 (2020).

[21] N. D. Khanh, T. Nakajima, X. Yu, S. Gao, K. Shibata, M. Hirschberger, Y. Yamasaki, H. Sagayama, H. Nakao, L. Peng, K. Nakajima, R. Takagi, T. Arima, Y. Tokura, and S. Seki, Nat. Nanotech. **15**, 444 (2020).

[22] M. Slaski, A. Szytula, J. Leciejewicz, and A. Zygmunt, J. Magn. Magn. Mater. **46**, 114 (1984).

[23] K. Hiebl, C. Horvath, P. Rogl, and M. J. Sienko, Sol. St. Commun. **48**, 211 (1983).

[24] A. Garnier, D. Gignoux, D. Schrnitt A', and T. Shigeoka, Phys. B **222**, 80 (1996).

[25] T. Samanta, I. Das, and S. Banerjee, J. Appl. Phys. **104**, 123901 (2008).

[26] F. Jonietz, S. Mühlbauer, C. Pfleiderer , A. Neubauer, W. Münzer, A. Bauer, T. Adams, R. Georgii, P. Böni, R. A. Duine, K. Everschor, M. Garst, and A. Rosch, Science **330**, 1648 (2010).

[27] T. Schulz, R. Ritz, A. Bauer, M. Halder, M. Wagner, C. Franz, C. Pfleiderer, K. Everschor, M. Garst, and A. Rosch, Nat. Phys. **8**, 301 (2012).

[28] G. Kimbell, C. Kim, W. Wu, M. Cuoco, and J. W. A. Robinson, Commun. Mater. **3**, 19 (2022).

[29] R. Takagi, N. Matsuyama, V. Ukleev, L. Yu, J. S. White, S. Francoual, J. R. L. Mardegan, S. Hayami, H. Saito, K. Kaneko, K. Ohishi, Y. Ōnuki, T. Arima, Y. Tokura, T. Nakajima, and S. Seki, Nat. Commun. **13**, 1472 (2022).

[30] N. D. Khanh, T.Nakajima, S. Hayami, S. Gao, Y. Yamasaki, H. Sagayama, H. Nakao, R. Takagi, Y. Motome, Y. Tokura, T. Arima, and S. Seki, Adv. Sci. **9**, 2105452 (2022).

[31] H. Hayashi, H. K. Yoshida, H. Sakurai, N. Kikugawa, and K. Yamaura, JPS Conf. Proc. **38**, 011103 (2023).

[32] K. Hiebl, C. Horvath, P. Rogl, and M. J. Sienko, Sol. St. Commun. **48**, 211 (1983).

[33] (Supplemental Materials) Magnetic susceptibility over a wide temperature range See Fig. S1.

[34] I. Felner and I. Nowik, J. Pyhs. Chem. Solids **45**, 419 (1984).

[35] (Supplemental Materials) See Fig. S2.

[36] T. Nomoto and R. Arita, J. Appl. Phys. **133**, 150901 (2023).

[37] (Supplemental Materials) See Fig. S3.

[38] A. Matsui, T. Nomoto, and R. Arita, Phys. Rev. B **104**, 174432 (2021).

[39] H. Oike, T. Ebino, T. Koretsune, A. Kikkawa, M. Hirschberger, Y. Taguchi, Y. Tokura, and F. Kagawa, Phys. Rev. B **106**, 214425 (2022).

[40] O. I. Utesov, Phys. Rev. B **103**, 064414 (2021).

[41] H. Yoshimochi, R. Takagi, J. Ju, N. D. Khanh, H. Saito, H. Sagayama, H. Nakao, S. Itoh, Y. Tokura, T. Arima, S. Hayami, T. Nakajima, and S. Seki, Nat. Phys. **20**, 1001 (2024).

[42] R. Oishi, Y. Shimura, K. Umeo, T. Onimaru, and T. Takabatake, J. Phy. Soc. Jpn. **91**, 124706 (2022).

[43] M. Bouvier, P. Lethuillier, and D. Schmitt, Phys. Rev. B **43**, 13137 (1991).

[44] J. A. Blanco, D. Gignoux, and D. Schmitt, Phys. Rev. B **43**, 13145 (1991).

[45] H. Hidaka, Y. Ikeda, I. Kawasaki, T. Yanagisawa, and H. Amitsuka, Phys. B Condens. Matter **404**, 3005 (2009).

[46] (Supplemental Materials) See Fig. S4.

[47] R. Mallik and E. V. Sampathkumaran, Phys. Rev. B **58**, 9178 (1998).

[48] (Supplemental Materials) See Fig. S5.

[49] M. Shatruk, J. Solid State Chem. **272**, 198 (2019).

[50] (Supplemental Materials) See Fig. S6.

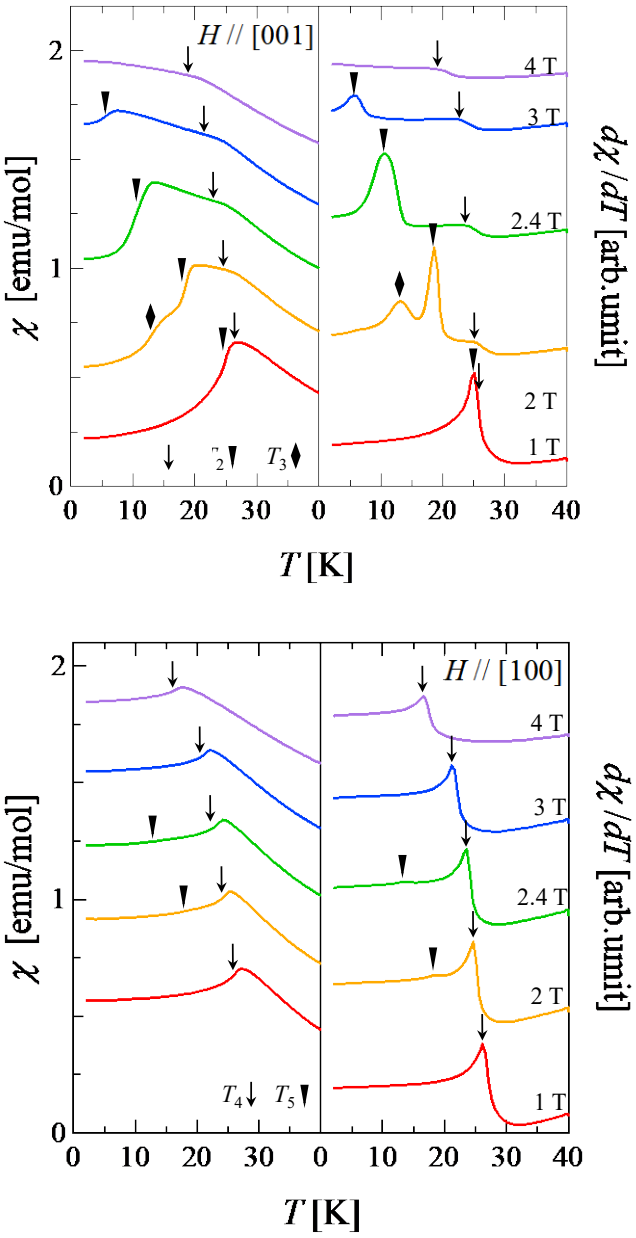

Fig. 1. (Color online) Temperature and field dependence of χ and its derivative (dχ/dT) for $GdOs_2Si_2$ measured with a magnetic field aligned along [001] (a) and [100] (b) directions. The arrows and different symbols denote characteristic magnetic transition temperatures: T_1, T_2, and T_3 for H//[001], and T_4 and T_5 for H//[100]. The data have been shifted for clarity.

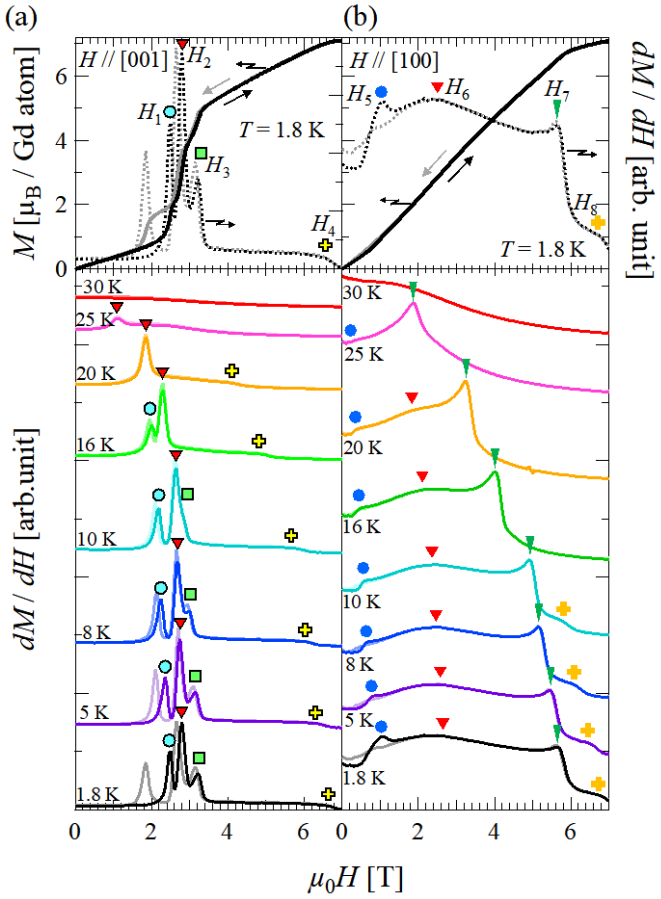

Fig. 2. (Color online) Isothermal magnetization curve (left axis) and its derivative dM/dH (right axis) measured at 1.8 K, with increasing and decreasing magnetic fields up to 7 T applied parallel to [001] (a) and parallel to [100] (b). The symbols represent critical fields: H_1, H_2, H_3, and H_4 for H//[001] and H_5, H_6, H_7, and H_8 for H//[100]. The thermal evolution of dM/dH is shown at the bottom. The data have been shifted for clarity.

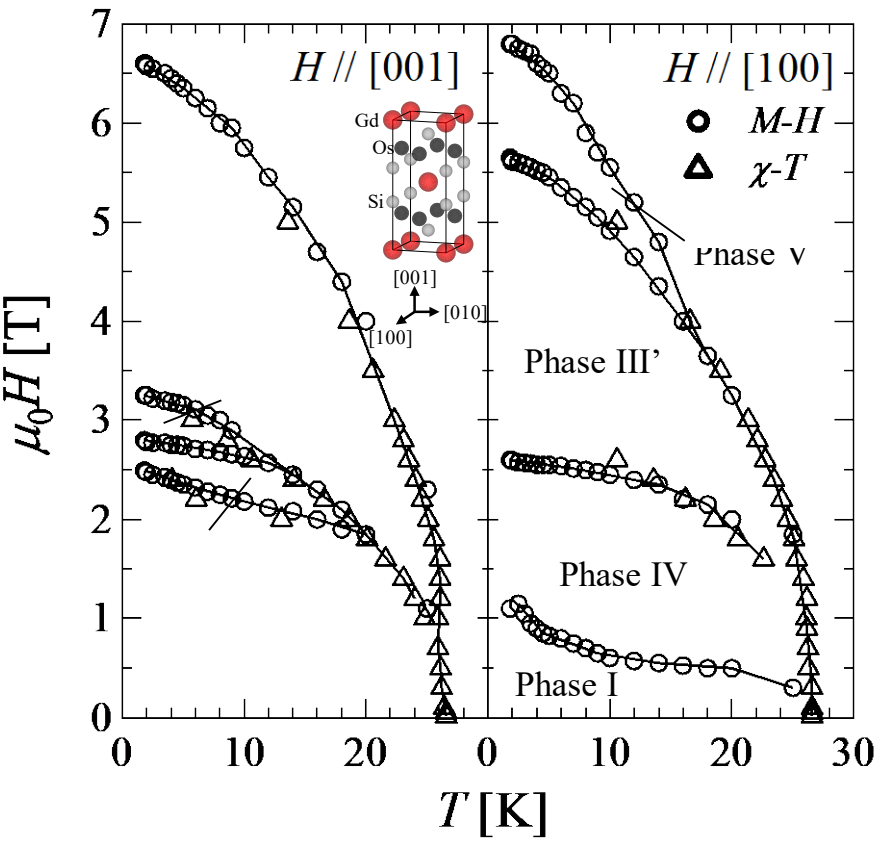

Fig. 3. (Color online) The magnetic field-temperature phase diagram for $GdOs_2Si_2$, with the magnetic field applied parallel to [001] (left) and [100] (right), based on magnetic measurements. The inset in the left figure depicts the crystal structure of $GdOs_2Si_2$, with red, black, and gray spheres representing Gd, Os, and Si atoms, respectively.

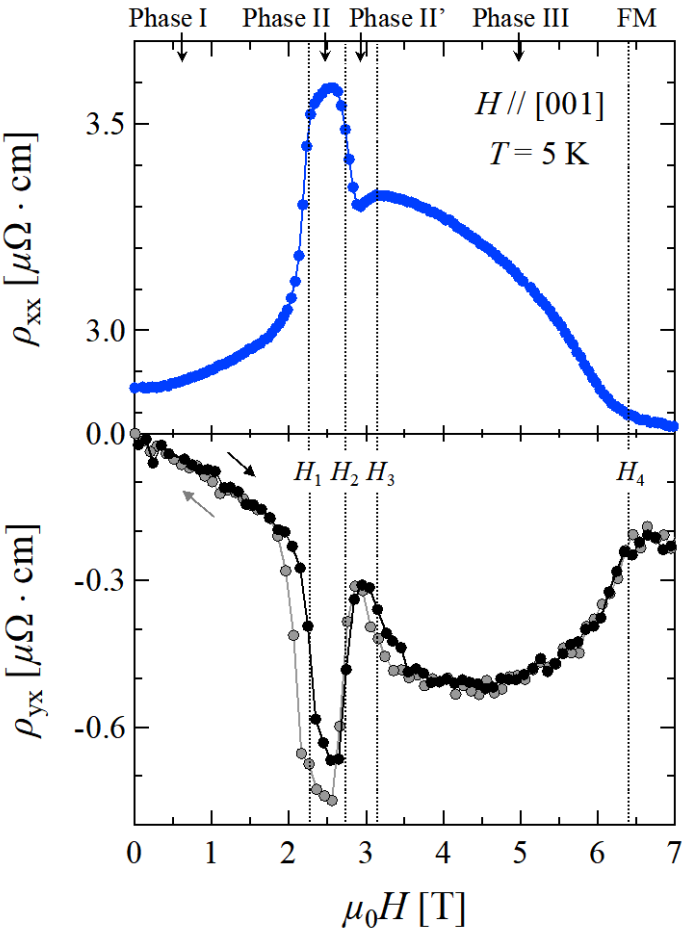

Fig. 4. (Color online) Magnetic field dependence of ρ_{yx} at 5 K for H//[001] and I//[100]. The black and gray curves represent ρ_{yx} with increasing and decreasing magnetic fields, respectively. The regions bordered by H_1 and H_2 (gray), H_2 and H_3 (yellow) correspond to the phases II and II', respectively.

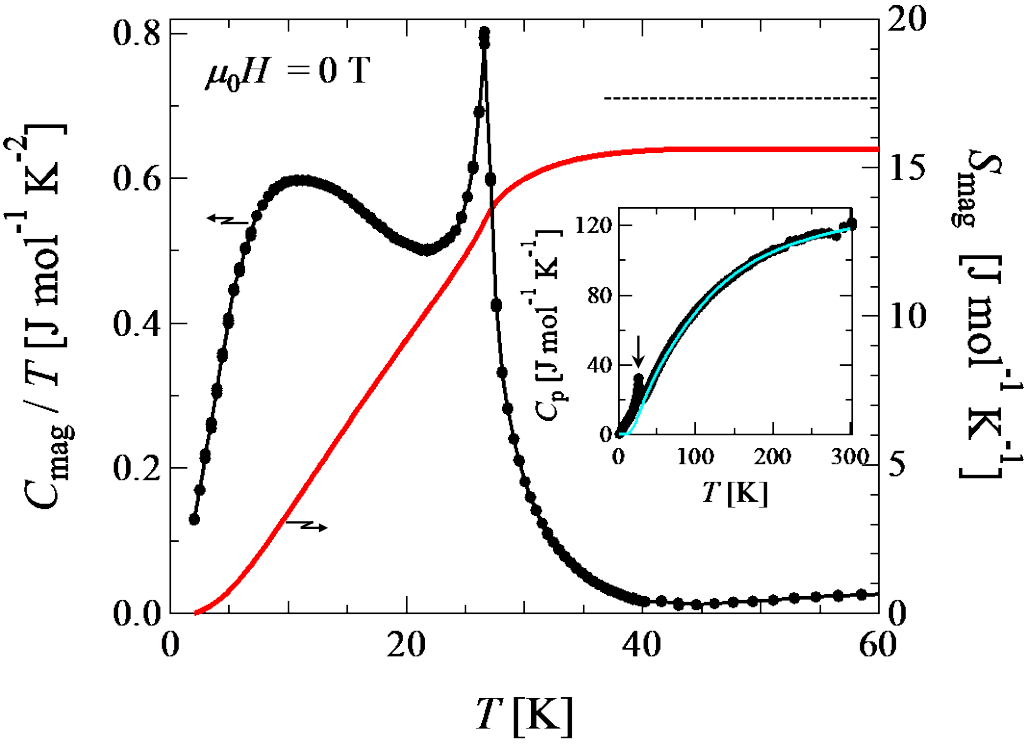

Fig. 5. (Color online) Temperature dependence of magnetic specific heat (C_{mag}) and magnetic entropy at $\mu_0 H = 0$ T. The inset displays the C_p-T data and the fitting curve (solid blue light line) obtained using the Einstein and Debye formula.